ACS APPLIED MATERIALS & INTERFACES

Research Article

www.acsami.org

Interfacial Investigation on Printable Carbon-Based Mesoscopic Perovskite Solar Cells with NiO_x/C Back Electrode

Fatemeh Behrouznejad,*[,†] Cheng-Min Tsai,[‡] Sudhakar Narra,[‡] Eric W.-G. Diau,*[,‡] and Nima Taghavinia*[,†,§]

[†]Department of Physics, Sharif University of Technology, Tehran 14588, Iran

[‡]Department of Applied Chemistry and Institute of Molecular Science, National Chiao Tung University, Hsinchu 30010, Taiwan

[§] Institute for Nanoscience and Nanotechnology, Sharif University of Technology, Tehran 14588, Iran

Supporting Information

ABSTRACT: Solar cells with high efficiency, low cost, and high stability are the target for the new generation of solar cells. A fully printable perovskite ($CH_3NH_3PbI_3$) solar cell (PSC) with device architecture FTO/TiO_2/Al_2O_3/NiO_x/C is fabricated in the current research as a low-cost and relatively stable structure and is investigated to determine how different fabrication factors such as the thickness of the insulating spacer layer (Al_2O_3) or treatments such as heat and UV−O_3 treatments can affect the interfacial properties of this multilayer mesoporous structure. X-ray photoelectron spectra (XPS) show that UV−O_3 treatment increases the Ni^{3+}(Ni_2O_3) phase on the surface of the black nickel oxide layer leading to better charge extraction and increasing open-circuit voltage (V_{OC}) up to 0.945 V. We observe improved $CH_3NH_3PbI_3$ formation inside the mesoporous layers by the PbI_2 penetration at a higher temperature. Impedance spectral together with current−voltage measurements show the effect of thickness for the insulator layer in the internal and interfacial resistances and photovoltaic characteristics of the cell. The best performance of the carbon-based PSC attains power conversion efficiency of 12.1% with the thickness of the Al_2O_3 layer at 450 nm.

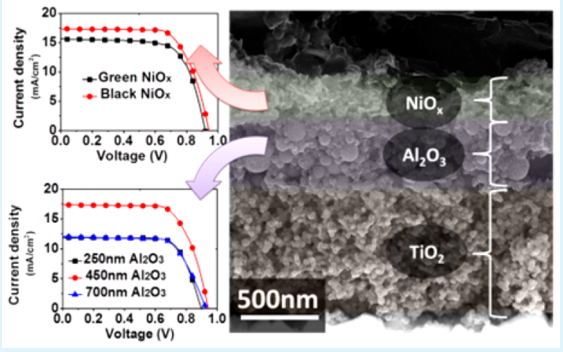

KEYWORDS: *perovskite-based solar cells, inorganic hole-transporting material, UV−O_3 treatment, impedance spectroscopy, open-circuit voltage, work function*

1. INTRODUCTION

The applications of organometallic halide perovskite materials (ABX_3, A = MA or FA; B = Pb or Sn; X = I, Cl, Br, or a combination of them) are in rapid progress for optoelectronic devices. These materials are known as promising energy materials for next-generation solar cells[1−3] and light emitting diodes[4,5] due to properties such as direct band gap absorption, high light-harvesting ability,[6,7] long carrier diffusion length (more than 100 nm to 1 μm),[8,9] relatively high carrier mobility (about 20 cm^2 /(V s)),[10] low excitonic binding energy,[2,8] and color-tunable appearance.[11] Furthermore, these materials can be formed in large crystal sizes with small defects using solution-based low-temperature fabrication methods. It seems that by overcoming the problem of stability, perovskites are promising materials for high-performance solar modules with a low-cost fabrication. Au and Ag are normally used as the back contact metals in perovskite solar cells (PSCs); however, the high cost of Au and low chemical stability of Ag[12] are major problems against commercialization of PSCs. Another important problem is the vacuum deposition of metals which is difficult for scale-up production. Organic hole-transporting materials (HTMs) such as 2,2′,7,7′-tetrakis(*N*,*N*-dimethoxyphenylamino)-9,9′-spirobifluorene (spiro-OMeTAD), poly(3-hexylthiophene-2,5-diyl) (P3HT), poly(3,4-ethylenedioxythiophene) poly(styrenesulfonate) (PEDOT:PSS),[13] and poly[bis-(4-phenyl)(2,4,6-trimethylphenyl)amine] (PTAA) are usually used in the conventional PSCs. Utilizing organic HTMs results in low stability and also high fabrication cost.[14] There are some reports that introduce HTM-free p-type $CH_3NH_3PbI_3$/Au structure,[15−18] and the best efficiency of 10.47% is reported.[18]

HTM-free carbon-based PSCs have been introduced recently to overcome these problems (a brief review of reported structures for PSCs with carbon electrode is reported in Table S1, Supporting Information (SI)). The carbon composite layer is used as a replacement for Au back contact electrodes. This structure was first introduced by Kay et al. in dye-sensitized solar cells (DSSCs) as a replacement for sandwich-type DSSCs, with an efficiency of 6.7%.[19] The manufacturing seems simpler relative to the conventional sandwich-type DSSC. However, the carbon composite layer must be thick with high porosity to

Received: February 25, 2017
Accepted: June 20, 2017
Published: June 20, 2017

DOI: 10.1021/acsami.7b02799
ACS Appl. Mater. Interfaces 2017, 9, 25204−25215

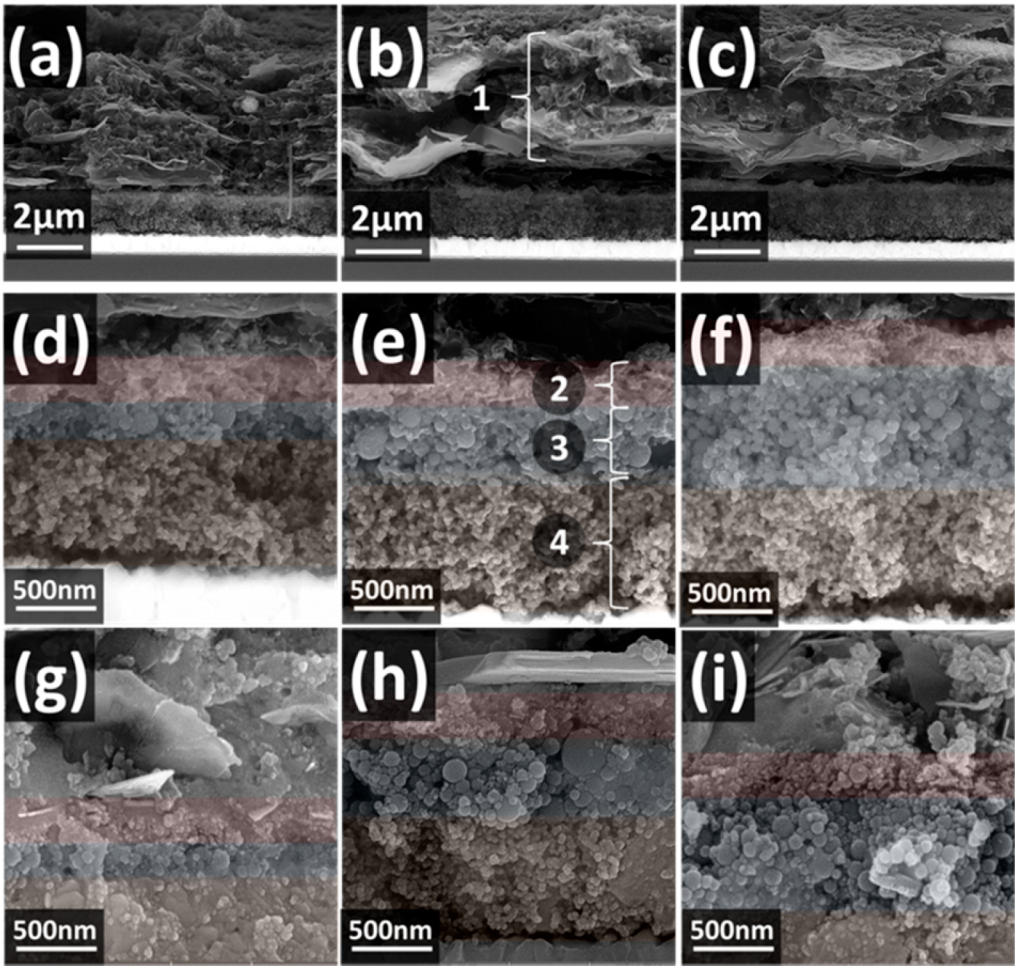

Figure 1. FESEM cross-sectional images of PSC showing device architectures with varied thicknesses of the Al_2O_3 layer: (a) 250, (b) 450, and (c) 700 nm before PbI_2 infiltration. Panels d–f show the corresponding side-view images of the device with a smaller scale bar than that shown in panels a–c. Panels g–i show the corresponding side-view device images after the formation of the perovskite layer inside the mesoporous structure. The thicknesses of TiO_2, NiO_x, and the carbon composite layer are about 700 nm, 300 nm, and 4 μm, respectively, for all devices. The carbon composite layer as a hole collector (panel b-1), NiO_x as an inorganic HTM (panel e-2), Al_2O_3 as an insulator spacer layer (panel e-3), and TiO_2 as an electron transport layer (panel e-4) are also indicated.

allow electrolyte and dye solution penetrating through the mesoporous structure. The thickness of the mesoporous TiO_2 layer should be more than 10 μm to adsorb sufficient dye molecules to harvest the solar light. This thick porous layer makes the whole device very brittle. By introducing perovskite materials as an active efficient light-harvesting medium, the thickness of the mesoporous TiO_2 layer can be decreased to less than 1 μm. Perovskite precursors can be dissolved in solvents and, therefore, can infiltrate into the mesoporous multilayer structure to form a robust device that significantly increases the mechanical stability of the cell. An efficiency of 6.64% was reported using this structure in PSCs for the first time by Ku et al.[20] and developed later[21−26] to attain PCE ∼ 15%.[26] In those reports, the thicknesses of the electron transport (TiO_2) and insulating spacer layers (ZrO_2 or Al_2O_3) were about 1 μm and effects on the film thicknesses with respect to the photovoltaic and interfacial characteristics of the devices have not yet been investigated in detail.

Another structure is lamination of carbon composites on the formed perovskite layer.[22,27−30] In this case the challenge is to choose the right solvent and deposition method, as this procedure can contaminate the perovskite layer. Different carbon composites using graphite, carbon black, and single-wall carbon nanotube (SWCN) were used to fabricate the back contact layer in PSCs. Li et al. indicated that laminating CNTs gives rise to an efficiency of 6.87% that increases to 9.90% by adding spiro-OMeTAD to the CNT network.[30] Habisreutinger et al. introduced a P3HT/SWCN-PMMA layer as a back contact electrode that also increases the cell's stability significantly.[31] Lamination after depositing the perovskite layer has the disadvantage of low contact area between the carbon electrode and the perovskite layer. Habisreutinger et al. had previously shown that using an organic HTM-free SWNT layer resulted in poor photovoltaic characteristics and attained an efficiency as low as 0.8%.[32] Cao et al. introduced thiolated nanographene as HTM in devices with the FTO/TiO_2/perovskite/HTL/Au structure to attain an efficiency of 12.81%.[33]

On the other hand, NiO or NiO_x,[34−39] CuI,[40] CuSCN,[41,42] and so on are potential inorganic HTMs that have been used in different types of PSCs.[43] Recently, it has been reported that the device performance of the carbon-based PSCs can be improved up to PCE 15% using NiO nanoparticles as an inorganic HTM layer.[35,37] An efficiency of 14.2% was obtained using NiO nanosheets.[44] Although this printable NiO/carbon-based PSC device structure has been reported elsewhere, the

DOI: 10.1021/acsami.7b02799
ACS Appl. Mater. Interfaces 2017, 9, 25204−25215

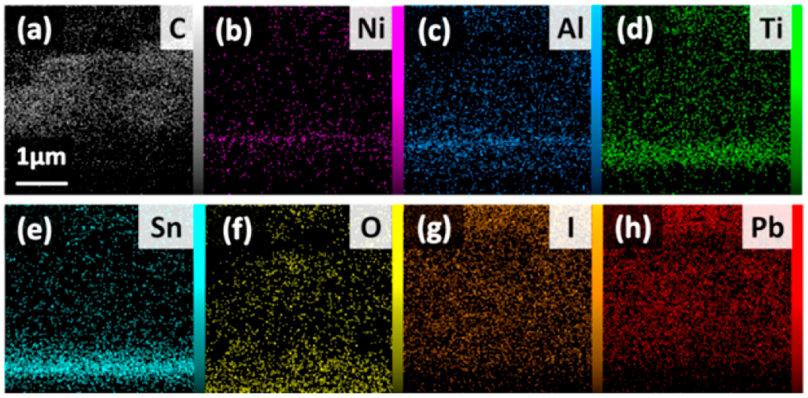

Figure 2. EDS mapping images for (a) C, (b) Ni, (c) Al, (d) Ti, and (e) Sn that are related to the carbon composite layer, NiO_x HTM layer, Al_2O_3 insulator layer, TiO_2 electron transporter, and FTO current collector layers, respectively. Panel f shows the EDS mapping image for O in NiO_x, Al_2O_3, and TiO_2 layers. Panels g and) show that PbI_2 was penetrated homogeneously through the mesoporous layers.

investigations for the effects of film thickness and surface treatments on photovoltaic performance seem to be necessary to further optimize the device performance. In the present study, the effect of the thickness of the Al_2O_3 layer on internal and interfacial resistances of the cell and photovoltaic characteristics are studied. Effects of heat and UV−O_3 treatments on performance improvements are also investigated.

2. EXPERIMENTAL SECTION

2.1. Fabrication of PSCs. *2.1.1. Preparation of Mesoporous Structure.* A compact TiO_2 thin film with the thickness of about 50 nm was deposited using spray pyrolysis method. Titanium (diisopropoxide) bis(2,4-pentanedionate) 75% in isopropanol (Sigma-Aldrich))/EtOH (1:15 volume ratio) solution was sprayed onto FTO substrates placed on a hot plate at 350 °C, followed by sintering in 500 °C for 30 min. The mesoporous TiO_2[39] layer was deposited by screen-printing TiO_2 nanoparticle paste (1 wt %) followed by heating at 125 °C (10 min), 325 °C (10 min), 375 °C (10 min), 450 °C (15 min), and 500 °C (30 min). The Al_2O_3 spacer layer was deposited by screen printing. The first layer is deposited by printing 2 wt % paste of Al_2O_3 (45 nm in diameter, Sigma-Aldrich). After heating at 125 °C (10 min), 325 °C (10 min), 375 °C (10 min), and 400 °C (30 min), the second Al_2O_3 layer is deposited by printing 2, 4, or 8 wt % Al_2O_3 paste to have insulator layers with different thicknesses. After heating with the same process, the NiO_x (Sigma-Aldrich) layer was printed using 2 wt % paste. The sintering process is the same as Al_2O_3 layer. A carbon composite layer is printed using carbon paste, which contains 5 wt % carbon black (Top Nano Technology, Taiwan), 5 wt % Al_2O_3 (Sigma-Aldrich), 10 wt % graphite (Homytech, Taiwan), 20 wt % ethyl cellulose (Sigma-Aldrich), and 60 wt % alpha-terpineol (Sigma-Aldrich). The thickness of this conductive layer is about 4−5 μm. Its heating procedure was the same as that of the Al_2O_3 layer.

2.1.2. Deposition of $CH_3NH_3PbI_3$. The perovskite deposition was done in a nitrogen-filled glovebox. A 40 wt % amount of PbI_2 solution (99%, Aldrich) in DMF (anhydrous, Aldrich) was prepared and stirred for 12 h on a hot plate in 70 °C. PbI_2 solution infiltrated and was kept at 70 °C. A 3 mL aliquot of this solution was dripped on the prepared mesoporous structures. The effect of sample temperature (room temperature or 70 °C) was also investigated. The PbI_2 infiltrated samples were kept at 70 °C for 30 min on a hot plate and then were immersed in methylamine iodide (MAI) solution (10 mg/mL in isopropyl alcohol (IPA; anhydrous, Aldrich) for 30 min. The sample then was rinsed with IPA and put on the hot plate at 70 °C for 30 min.

2.2. Characterizations. The black nickel oxide powder was studied using X-ray diffraction (XRD) characterization. The effect of UV−O_3 treatment on the surface composition of deposited nickel oxide layer was investigated by X-ray photoelectron spectroscopy (XPS; Specs-EA10+) with an Al X-ray source.

Diffuse reflectance spectra were measured using an Avantes spectrometer. Cross-sectional images of PSCs before and after $CH_3NH_3PbI_3$ deposition were taken by field emission scanning electron microscopy (TESCAN-MIRA3-XM). Energy dispersive spectra (EDS) were also measured to evaluate the film uniformity using this instrument.

Current density−voltage measurements were done under AM1.5 intensity Solar-simulator (XES-40S1, SAN-E1) and Keithly 2400 digital source meter. Incident photon-to-current conversion efficiency was measured using a Xe lamp (PTiA-1010, 150 W) and a monochromator (PTi). The internal resistances of the PSCs were measured by impedance spectroscopy using an Autolab potentiostat instrument under light with different intensities (using Sharif solar simulator).

Time-resolved photoluminescence (TRPL) decay transients were recorded with a time-correlated single-photon-counting (TCSPC) system (Fluotime200, PicoQuant) using a 635 nm ps pulsed-diode laser (LDH-635, PicoQuant, fwhm ∼ 70 ps) as excitation source; the PL temporal profiles were collected at 770 nm. The pulse energy used for excitation was 15 $\mu J\ cm^{-2}$.

3. RESULTS AND DISCUSSION

3.1. Solar Cell Structure. The cross-sectional FESEM images of the printed mesoporous structure of the TiO_2/Al_2O_3/NiO_x/C composite with different thicknesses of Al_2O_3 are shown in Figure 1. The TiO_2 layer with thickness 700 nm was prepared using nanoparticles with a size of 20 nm in diameter. TiO_2 is a well-known n-type material with an electron affinity of 4.1 eV and bandgap of 3.2 eV to serve as a good electron transporter and hole-blocking layer in optoelectronic devices. NiO_x nanoparticles with a size 30 nm in diameter were used for producing the HTM layer with thickness of about 300 nm. NiO_x has proper valence band energy (5.4−5.6 eV) to be an inorganic HTM for $CH_3NH_3PbI_3$-based solar cells and also has proper conduction band energy (1.5−2.1 eV) with the bandgap of 3.5−4.0 eV[34] to be an electron-blocking layer.

A composite of flakes of graphite and carbon black was used as a back contact material. The reported carrier concentration in the pure graphite is about $10^{18}\ cm^{-3}$.[45] The work function is a critical parameter to choose the right components for utilizing in the carbon composition. In the case of CNTs, it is shown that by increasing the CNT diameter from 0.48 to 1.43 and 5.32 nm, the energy gap decreases from 1.497 to 0.500 and 0.135 eV; the intrinsic carrier concentrations increase from $1.239 \times 10^9/cm^3$ to $5.530 \times 10^{16}/cm^3$ and $9.924 \times 10^{18}/cm^3$, respectively; that change was in a wide range.[46] CNT was introduced as a p-type semiconductor with the work function

DOI: 10.1021/acsami.7b02799
ACS Appl. Mater. Interfaces 2017, 9, 25204−25215

between −4.95 and −5.05 eV, but its hole extraction is weaker than its composition with spiro-OMeTAD.[47] The work function of amorphous carbon was reported to be −4.8 eV[47] while that of pure graphite was reported to be −5.0 eV;[48] therefore it seems that flaky graphite−carbon black structure is a good choice for utilization as a back electrode.

To avoid contact between the carbon composite and the TiO_2 layer, a thin layer of mesoporous Al_2O_3 layer was deposited onto the mesoporous TiO_2 layer. In the conventional carbon-based structure, the thickness of this insulator layer can be a critical parameter. The mesoporous structures after formation of the $CH_3NH_3PbI_3$ dense layer are also demonstrated in Figure 1g−i for the thicknesses of the Al_2O_3 layer with 250, 450, and 700 nm, respectively. The most important advantage of this structure is that all layers are printable and the perovskite deposition is done at the end of the fabrication procedure; therefore metal oxide and carbon pastes can be fabricated with different solvents that will not affect the deposition of the perovskite layer inside the mesoporous structure. This is a limiting factor in selecting HTM and electron-transporting material (ETM) in other structures. Cross-sectional energy dispersive spectral data (EDS) of the devices indicate that by utilizing the screen-printing method, all mesoporous layers (TiO_2, Al_2O_3, NiO_x, and carbon composite layers) are deposited neatly onto each other and PbI_2 is penetrated homogeneously through them (Figure 2).

3.2. NiO_x Layer. Frenkel defects in metal oxides determine their semiconducting types. Most of metal oxides such as TiO_2 and ZnO are n-type semiconductors due to oxygen defects as anion vacancy for electrons to occupy in their conduction bands, but defects in NiO_x structure are cation vacancy defects. NiO is an insulator at 0 K. By increasing the temperature, removal of some Ni atoms from their sites in the lattice results in increasing the number of oxygen atoms around other adjacent nickel atoms; therefore, Ni^{2+} oxidized to Ni^{3+}; in this case the structural stoichiometry changes from NiO to NiO_x (with more percentage of Ni_2O_3).[49] The conductivity of the nickel oxide layer is attributed to hole hopping from Ni^{3+} sites to Ni^{2+} sites. Here we use both black and green powder of nickel oxide as initial powders to make the NiO_x pastes. The same powder size was used to have a correct comparison (Figure S1a−c).

The X-ray diffraction pattern of black powder is shown in Figure 3. By increasing the number of defects and changing the stoichiometry, the color of nickel oxide changes from green to black; nevertheless the peak list that is shown in Figure 3b (upper figure) compared to XRD reference peak list of NiO, $Ni(OH)_2$, NiOOH, and Ni_2O_3 indicated that the black material structure inside our device is similar to that of NiO; therefore we can conclude that the difference between the black and green powders is due to the surface compositions and structures. The size of crystallites with Debye− Scherrer relation is about 20−25 nm.

It is shown that utilizing a nickel oxide layer between Al_2O_3 and the carbon composite layer results in fast charge extraction and "shifting hole Fermi-level down"; therefore, the open-circuit voltage (V_{OC}) value increases.[35] The simulation results of the band diagram of the PSCs with and without NiO using SCAPS software are illustrated in Figure 4. As the initial parameters for the modeling, the effective mass of electrons in the conduction band of TiO_2 is between 5 and 10 m_0,[50] while that of electrons and holes in the $CH_3NH_3PbI_3$ lattice is

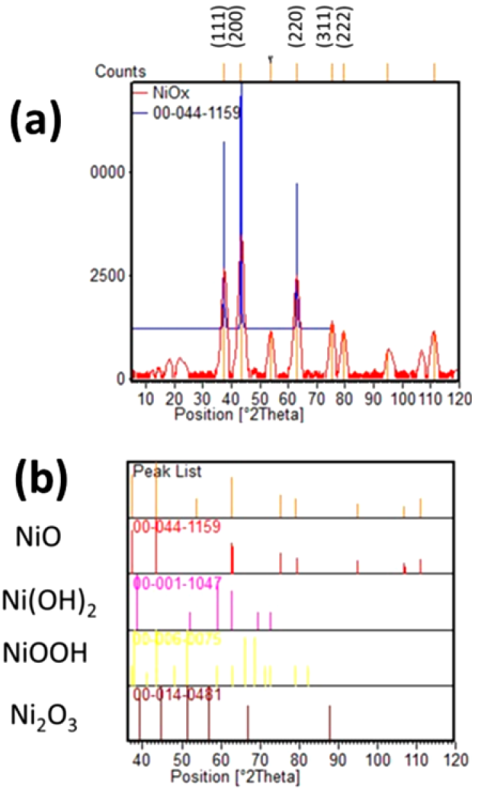

Figure 3. (a) X-ray diffraction spectrum of the black nickel oxide powder in comparison with that of the reference spectrum obtained from the green NiO powder; (b) peak list of the sample compared to the reference peak lists for NiO, $Ni(OH)_2$, NiOOH, and Ni_2O_3.

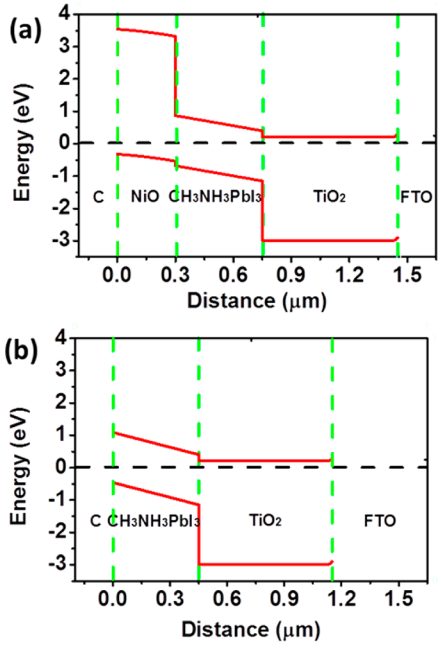

Figure 4. Calculated band bending of printable PSC with (a) nickel oxide as an inorganic HTM and (b) that of HTM-free PSC (by SCAPS software).

reported to be about 0.15 m_0 and 0.18 m_0,[51] respectively. The effective mass of holes in a NiO single-crystal lattice is reported to be about 1 m_0.[52] This diagram indicates that the nickel oxide facilitates the hole extraction by decreasing the difference

DOI: 10.1021/acsami.7b02799
ACS Appl. Mater. Interfaces 2017, 9, 25204−25215

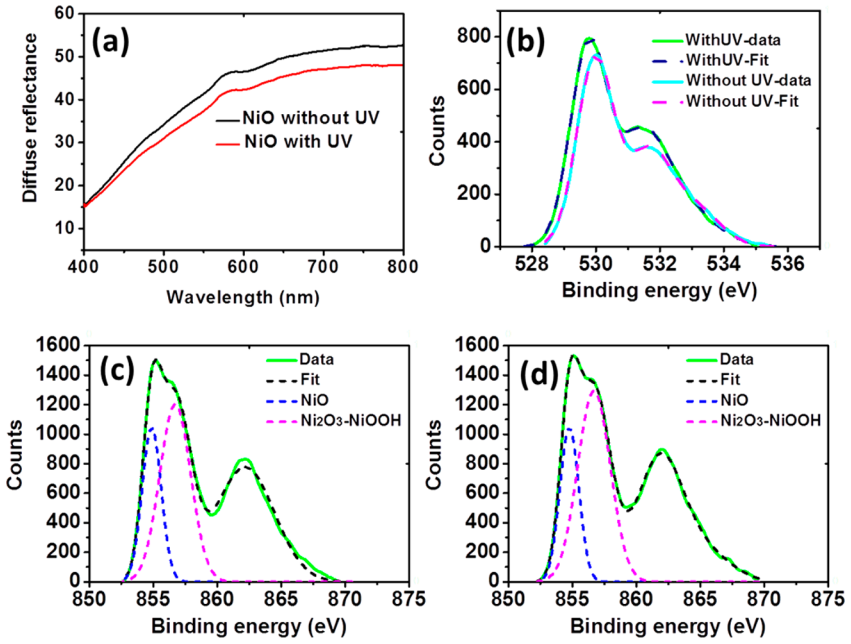

Figure 5. Spectra of (a) diffuse reflectance and XPS results related to the mesoporous NiO_x layer (c) before and (d) after UV−O_3 treatment. The oxygen peaks are compared in panel b; the left peak is attributed to binding energy in NiO, and the right one is attributed to binding energy in Ni_2O_3. The deconvoluted Ni peaks before and after UV−O_3 treatments are shown in panels c and d, respectively.

between the valence band energy level of the last layer and the Fermi level of the carbon layer that gives rise to decreasing energy dissipation and also reduces the recombination at the perovskite/carbon interface. This figure indicates that the nickel oxide acts as a good electron barrier layer.

3.3. Effects of UV−O_3 Treatment. By utilizing UV−O_3 treatment on NiO layers V_{OC} increases in average from 0.90 to 0.94 V. In addition to the substrate cleaning, UV−O_3 treatment is also effective in tuning the work function. It was reported that UV−O_3 treatment forms dipoles on the surface of ITO, ZnO, and PEDOT:PSS, enhancing charge transfer properties.[53,54] Lee et al. showed that the work function of PEDOT:PSS increased from 5.00 to 5.25 eV after treatment by UV−O_3 for 60 min, and the specific resistance decreased from 0.72 to 0.39 MΩ cm.[53] Liu et al. reported that UV−O_3 treatment can change the morphology and stoichiometry of solution processed NiO_x films utilized in OLEDs. They showed that $Ni(OH)_2$ is converted to NiOOH on the surface.[55]

Kim et al. reported the positive effect of this treatment on increasing conductivity of Cu-doped nickel acetate layer which was utilized as an underlayer for the perovskite film.[54]

To investigate the UV−O_3 effect on increasing V_{OC} in this research, a thin layer of NiO was deposited on a glass substrate, and after sintering, the diffuse reflectance spectra were measured before and after UV−O_3 treatment. The layer looks darker after this treatment with more than 5% inferior diffuse transmittance (Figure 5a). The shape also changes as a result of changing surface composition. The layers become lighter after aging for some hours. The nickel oxide surface could be changed during the UV−O_3 treatment according to the following reactions.[56]

$$O_3 + H_2O + h\nu \rightarrow 2OH + O_2 \quad (1)$$

$$NiO + OH^- \rightarrow NiOOH + e^- \quad (2)$$

During this process Ni(II) changes to Ni(III) on the surface. Formation of NiOOH results in layer darkening. The band gap change also confirms the surface chemical changes. Postheating gives rise to removal of hydroxyl groups and converting NiOOH to Ni_2O_3[57] (after some hours the color looks lighter due to this reaction). Hence, by this treatment the content of Ni_2O_3 of the nickel oxide layer increases to some extent. X-ray photoelectron spectra (XPS) were measured to study the surface composition of nickel oxide film (Figure 5b−d). The Ni(2p) peak is deconvoluted to Ni^{2+} and Ni^{3+} peaks at 854.8 and 856.5 eV as shown in Figure 5c,d, respectively, consistent with those reported elsewhere.[58] The wider peak in higher energy is a satellite peak.[58] The XPS shows that the area under the Ni(III) peak increases due to the change of surface stoichiometry and the increasing area of related oxygen peak (right peak shown in Figure 5b and Figure S2, SI) confirm this result.

The green nickel oxide layer converts to black after annealing at 400 °C and looks darker after treating by UV−O_3. Utilizing the green nickel oxide in a PSC structure results in inferior V_{OC}, lower short-circuit current−density (J_{SC}) and therefore inferior efficiency (h) relative to the black NiO (Figure S3 and Table S2, SI). It seems that the hole extraction is enhanced and the Fermi-level energy is lowered, and this gives rise to increasing V_{OC} in the case of black NiO. The reported work function of Ni_2O_3 is 5.4 eV.[59] Although heating in air changes the color of green nickel oxide due to producing cation vacancy defects but inferior efficiency indicated that internal parts of the NiO nanoparticles do not change significantly.

3.4. Effects of the PbI_2 Deposition Temperature. The $CH_3NH_3PbI_3$ layer was deposited by the sequential method. The temperature is a critical parameter for a good film formation. The PbI_2 was dripping on the multilayer film structure at room temperature (about 25 °C) in comparison with film placed on a hot plate at the temperature 70 °C. The FESEM images of the filled PbI_2 layers are shown in Figure 6. Although the deposition at room temperature results in good penetration and formation of a dense PbI_2 layer through the mesoporous structure (Figure 6a), the dense PbI_2 inhibits

DOI: 10.1021/acsami.7b02799
ACS Appl. Mater. Interfaces 2017, 9, 25204−25215

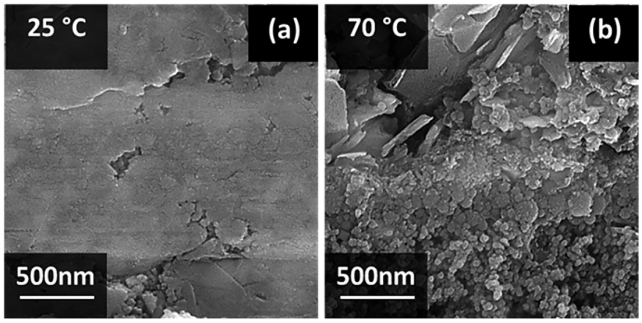

Figure 6. Cross-sectional FESEM images of penetrated PbI_2 through the mesoporous structure that was kept (a) at room temperature compared to (b) at the temperature of 70 °C.

effective penetration of MAI and formation of the perovskite phase, giving rise to poor device efficiency and reproducibility. The penetration temperature of 70 °C is therefore the optimal infiltration condition in terms of device performance (Figure S4 and Table S3, SI).

3.5. Device Characterization. The current density–voltage curves and the efficiency of incident photon-to-current conversion (IPCE) of the PSCs are demonstrated in Figure 7 and Table 1 in average (the results are reported in Tables S3–S5 in detail). The forward and backward curves are demonstrated in (Figure S5, SI) in comparison with each other.

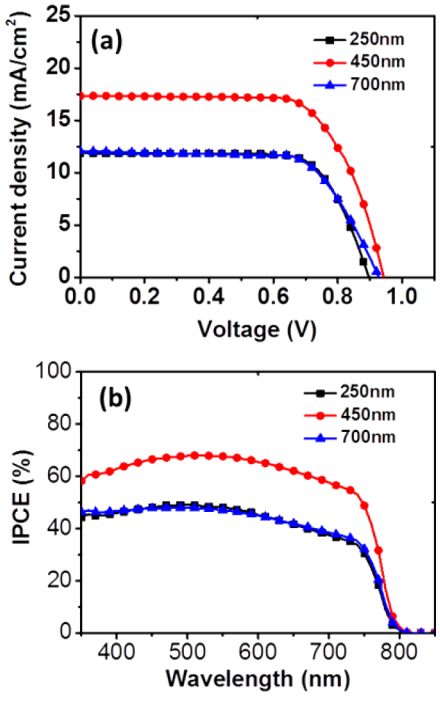

Figure 7. (a) Current density–voltage characteristic curves and (b) IPCE action spectra for carbon-based PSCs with varied thicknesses of the Al_2O_3 layers as indicated.

The results indicate that the thickness of the Al_2O_3 spacer layer is a critical parameter to be considered in the performance of the device. As shown in Figure 7a,b, the best device performance was achieved at the Al_2O_3 layer with film thickness of 450 nm. It seems that the recombination probability increases when the spacer layer is too thin or too thick.

Table 1. Photovoltaic Characteristics of PSCs with NiO_x/Carbon Electrode with Different Thicknesses of Al_2O_3 Layer[a]

thickness of Al_2O_3 layer (nm)	$J_{SC(av)}$ (mA/cm^2)	$V_{OC\ (ag)}$ (mV)	$FF_{(av)}$	PCE_{av} (%)	PCE_{max} (%)	S (%)
250	11.58	898	0.73	7.65	8.03	0.62
450	17.22	945	0.69	11.28	12.12	0.66
700	12.60	913	0.66	7.51	7.69	0.18

[a]The standard variation is reported in the last column.

Electrochemical impedance spectra (EIS) were measured from 0.01 Hz to 1 MHz under different light intensities (open-circuit voltages from 0.1 to 0.95 V) to investigate the internal resistivity of PSCs; the results are shown in Figure 8. Complete analysis of EIS is difficult due to the complicated three-dimensional structure, forming multiple layers and interfaces. The equivalent circuit of PSCs in DC mode is illustrated in Figure 8a. The shunt resistance is related to all recombination phenomena at the interfaces and layers of the device which is in parallel with the diode. The series resistance contains an external series resistance (resistance of substrates and contacts), and an internal series resistance (related to transfer and transport resistances in the PSC structure) is shown by R_s in Figure 8a. The interfacial impedances of the PSC are conventionally simulated using a resistance element parallel with a constant phase element (CPE) which represents the charge separation at the interface. As shown in Figure 8d–i, five semicircles are indicated in the impedance spectra, especially in relatively higher bias voltages. A resistance in parallel with a CPE can be used for fitting each of these curves. It is known that the value of p in the CPE impedance formula ($T^{-1}\omega^{-p}$) approaches 1 for films with low defects and grain boundaries. In spacer-free perovskite solar cells with and without a mesoporous layer, this value approaches 1.[60] In the case of this fully mesoporous structure, p values are between 0.6 and 0.8. This shows that the present PSC structure possesses the highest density of surface defects compared to the conventional PSC structures, and its EIS data interpretation might be more complicated than the conventional device structures.

Possible models to be considered for EIS data interpretation are shown in Figure 8b,c. The model in Figure 8c is a contracted form of the model in panel b, where the transport resistivity of the films is neglected.

The first semicircle in the Nyquist plot is attributed to the charge transfer phenomena at the interface of C/NiO_x. Utilizing flake of graphite and also carbon black in the carbon composite layer provides a higher contact area with the mesoporous nickel oxide layer filled by the perovskite nanocrystals and this is effective in decreasing interfacial charge transfer resistance. An electron transport resistance attributed to transport through TiO_2 nanoparticles is sometimes considered in analyzing impedance spectra of solar cells with mesoporous structures. This transport resistance was not observable in our previous investigations[61–63] due to the good interconnection between TiO_2 nanoparticles as a result of sintering at 500 °C. The main important difference between these cells is the thickness of the porous Al_2O_3 layer as an insulator spacer layer. The charge carriers transport through the perovskite layer that fills the spacer layer; therefore a transport resistance can be attributed to the perovskite layer (Figure 8b).

DOI: 10.1021/acsami.7b02799
ACS Appl. Mater. Interfaces 2017, 9, 25204–25215

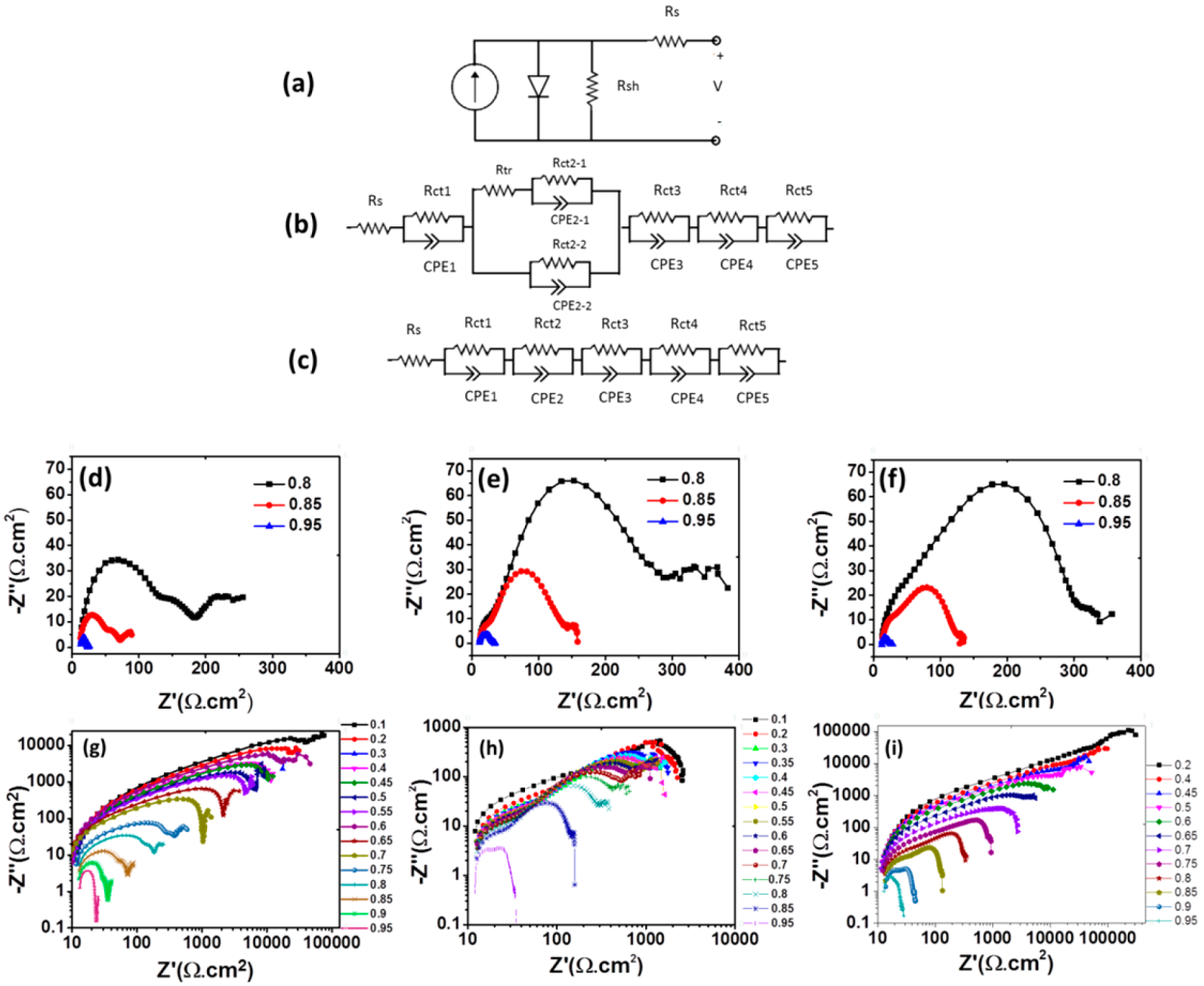

Figure 8. (a) DC and (b, c) AC equivalent circuits and (d–i) EIS data for printable PSC with carbon contact and impedance spectra related to PSCs with 250, 450, and 700 nm thickened Al_2O_3 layers in different open-circuit voltages (under light illumination). The equivalent series and shunt resistances are indicated by R_s and R_{sh}, respectively, in panel a. In the AC equivalent circuits (b, c), the resistances of substrates and contacts are indicated by R_s and the transport resistance through perovskite material by R_{tr}. A resistance in parallel with a constant phase element (CPE) is defined for each interface (R_{ct1}/CPE1 for C/NiO_x, R_{ct2}/CPE2 for NiO_x/$CH_3NH_3PbI_3$, and R_{ct3}/CPE3 for $CH_3NH_3PbI_3$/TiO_2 interfaces). The last two parallel elements can be attributed to slow phenomena such as ion migration through different layers. In the AC circuit shown in panel b, the R_{ct2-2} is attributed to recombination resistance, when there are undesired connections between the carbon layer or HTM and TiO_2, this resistance decreases. In contrast, in a well-fabricated cell, R_{ct2-2} is a relatively big resistance in comparison with the R_{ct2-1} and the AC equivalent circuit model can be represented by panel c.

According to the fitting results (using the AC circuit shown in Figure 8b) the transport resistance related to perovskite layers with thicknesses of 300, 450, and 700 nm is 1, 5, and 25 Ω cm^2, respectively (Figure S6b, SI). A path bypassing the perovskite layer can be considered, for instance due to penetrating NiO_x and a carbon composite layer through the holes of the spacer layer and contact formation with the TiO_2 layer, as shown in Figure 8b (R_{ct2-2}).

A CPE can also be attributed to this interface (CPE2–2). The measured internal resistances by fitting the impedance spectra at high light intensities using the circuit shown in Figure 8b are indicated in Figure S6b–e, SI. R_{ct-2-1} and R_{ct-2-2} are not distinguishable in lower light intensities, and the magnitude of R_{tr} is negligible in comparison with other impedances; therefore the second equivalent circuit (Figure 8c) is considered as a global model for all voltages from 0.1 to 0.95 V.

In the case of the NiO_x mesoporous layer, it seems that the transport resistance is also negligible due to sintering at 400 °C and its relatively high mobility. The mobility of 500 °C annealed NiO_x is reported between 0.14 and 0.43 $cm^2/(V\ s)$,[55] which is significantly higher than that of the device fabricated with good organic HTMs such as single-crystal spiro-OMeTAD (0.0013 $cm^2/(V\ s)$).[64]

Electronic polarizations are fast and must be investigated at the high-frequency regions. Therefore, the first three curves at higher frequencies can be attributed to polarization at the interfaces of C/NiO_x, NiO_x/$CH_3NH_3PbI_3$, and $CH_3NH_3PbI_3$/TiO_2, respectively. In contrast, ionic polarizations are slow[65] and fourth and fifth curves can be attributed to these slow phenomena. These slow phenomena are not discussed in this research. The semicircles in the intermediate frequency region are attributed to interfaces of perovskite with its adjacent materials.[42,66] The semicircle of HTM/$CH_3NH_3PbI_3$ interface is normally reported on the left side of that of the TiO_2/$CH_3NH_3PbI_3$ interface (for instance spiro-OMeTAD or PEDOT:PSS). Transient photoluminescence tests also dem-

DOI: 10.1021/acsami.7b02799
ACS Appl. Mater. Interfaces 2017, 9, 25204–25215

onstrate that the charge transfer through HTM is faster. In the case of the $NiO_x/CH_3NH_3PbI_3$ interface, it is indicated that charge transfer can be faster and slower than that of the $TiO_2/CH_3NH_3PbI_3$ interface for an 80 nm thick continuous layer of NiO_x[39] and 1.4 μm thick mesoporous NiO nanosheets,[44] respectively. Therefore, distinguishing the $TiO_2/CH_3NH_3PbI_3$ semicircle from $NiO_x/CH_3NH_3PbI_3$ is not straightforward. The semicircles in the intermediate frequency region are attributed to interfaces of perovskite with its adjacent materials.[42,66] The semicircle of $HTM/CH_3NH_3PbI_3$ interface is normally reported on the left side of that of the $TiO_2/CH_3NH_3PbI_3$ interface (for instance spiro-OMeTAD or PEDOT:PSS). Transient photoluminescence tests also demonstrate that the charge transfer through HTM is faster. In case of the $NiO_x/CH_3NH_3PbI_3$ interface, it is indicated that charge transfer can be faster and slower than that of the $TiO_2/CH_3NH_3PbI_3$ interface for an 80 nm thick continuous layer of NiO_x[39] and 1.4 μm thick mesoporous NiO nanosheets,[44] respectively. Therefore, distinguishing the $TiO_2/CH_3NH_3PbI_3$ semicircle from $NiO_x/CH_3NH_3PbI_3$ is not straightforward. Time-resolved PL experiments were performed using time-correlated single-photon-counting (TCSPC) technique to determine the intrinsic lifetimes of perovskite and its interfacial electron/hole transfer kinetics in this work (Figure 9). Perovskites were

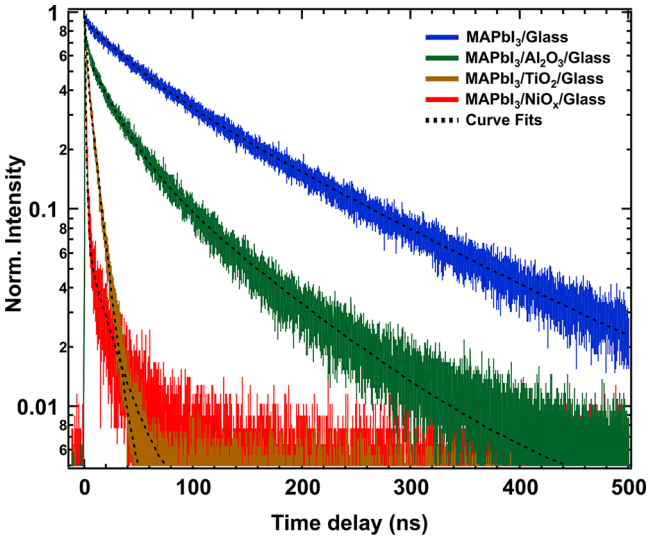

Figure 9. TCSPC decay profiles of $MAPbI_3$ deposited on glass, Al_2O_3, TiO_2, and NiO_x, respectively. The films were excited using a 635 nm picosecond diode laser, and emission is detected at 770 nm.

deposited using a two-step sequential method on glass and on varied metal oxide scaffolds (The samples are glass/perovskite, glass/Al_2O_3/perovskite, glass/TiO_2/perovskite, and glass/NiO_x/perovskite). The thickness of the perovskite is about 300 nm on glass and about 1000 nm on the Al_2O_3 scaffold. The average lifetime of perovskite is 109.5 ns on glass and 52.5 ns on the Al_2O_3 scaffold. The shortening of the lifetime of perovskite on the Al_2O_3 scaffold could be due to more recombination centers generated inside the compact crystal network and greater thickness of the film. The lifetimes of perovskite deposited on TiO_2 or NiO_x mesoporous layers showed considerable reduction in lifetimes compared to those of the perovskite samples deposited on glass or on the Al_2O_3 scaffold; the average lifetimes of the perovskite/TiO_2 and the perovskite/NiO_x samples are 6.4 and 2.4 ns, respectively. The reduction in their lifetimes of these films are due to their interfacial electron/hole transfer from the corresponding perovskite films to either the n-contact TiO_2 layer or the p-contact NiO_x layer. The electron transfer and hole transfer time constants are estimated to be 6.8 and 2.5 ns, respectively (Table 2).

Table 2. Lifetimes (Relative Amplitudes) of Perovskite Deposited on Different Underlayers

sample	τ_1 (ns) (A_1)	τ_2 (ns) (A_2)	τ_{PL} (ns)	τ_e (ns)	τ_h (ns)
Psk	44.7 (0.39)	151 (0.61)	109.5	–	–
Psk/Al_2O_3	26.2 (0.63)	97.4 (0.37)	52.5	–	–
Psk/TiO_2	2.0 (0.34)	8.7 (0.66)	6.4	6.8	
Psk/NiO_x	1.2 (0.94)	21.5 (0.06)	2.4		2.5

The average lifetime τ_{PL} is estimated using the amplitude weight-average formula which is given by

$$\tau_{PL} = \frac{\sum_{i=1}^{n} a_i \tau_i}{\sum_{i=1}^{n} a_i} \quad (3)$$

The interfacial electron or hole transfer time is estimated using the following formula:

$$\frac{1}{\tau_{e(or)h}} = \frac{1}{\tau_{Psk/ETL(or)HBL}} - \frac{1}{\tau_{Psk}} \quad (4)$$

The shape of the measured interfacial resistances versus V_{OC} is not very different for $TiO_2/CH_3NH_3PbI_3$ and $NiO_x/CH_3NH_3PbI_3$ interfaces so that the assignment on those semicircles to be due to either the $TiO_2/CH_3NH_3PbI_3$ or the $NiO_x/CH_3NH_3PbI_3$ interface does not change our discussion, For this reason we labeled these fitted values as R_{p1}, CPE_{p1}, R_{p2}, and CPE_{p2}, respectively.

The physics of R_{p1} or R_{p2} has been interpreted differently in the literature. In some works it is attributed to charge transfer phenomena and it is indicated that decreasing this resistance gives rise to efficiency enhancement,[42,66] but in some other works, this resistance is attributed to charge recombination and it is indicated that increasing this resistance results in efficiency enhancement. Ye et al. reported that in the case of PSC with a nonuniform perovskite film and more current leakage the charge transfer resistances measured by EIS increase while shunt resistances measured using the current density−voltage curve decrease.[42] Yang et al. reported lower charge transfer resistance for the carbon-based cathode that has a better contact with the perovskite layer.[66] It seems that interpreting the interfacial resistance as charge transfer resistance with the meaning of resistance against transferring charge carriers in the desired way or resistance against transferring charge carriers in the opposite direction as recombination resistance is not precise, e.g., the built-in potential that is produced at the $CH_3NH_3PbI_3/TiO_2$ interface results in transferring electrons from $CH_3NH_3PbI_3$ to TiO_2 but produces a recombination resistance against transferring electrons in the opposite direction (from TiO_2 to $CH_3NH_3PbI_3$).

In the case of the present study, the calculated parameters for the PSCs with different thicknesses of Al_2O_3 layer are shown in Figure 10. The work function of NiO_x is about −5.4 eV,[38] which gives rise to an ohmic contact with the carbon composite layer and relatively low interfacial resistance (Figure 10a). In this work, for the 450 nm thick Al_2O_3 layer, the consequent resistance at the interface of TiO_2 and $CH_3NH_3PbI_3$ remains

DOI: 10.1021/acsami.7b02799
ACS Appl. Mater. Interfaces 2017, 9, 25204−25215

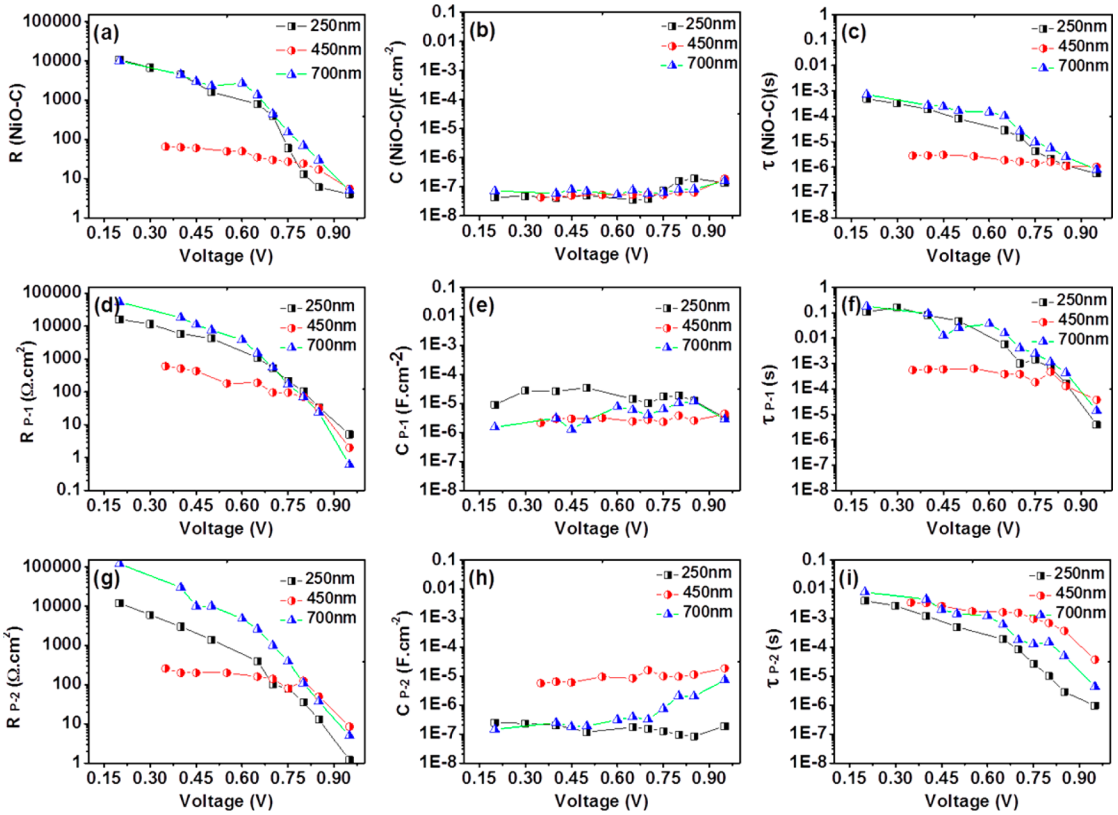

Figure 10. (a) Charge transfer resistance, (b) capacitance (where, for example, 1E-3 represents 1×10^{-3}), and (c) related constant time for the NiO_x/C interface calculated by fitting the impedance spectra of PSCs by the equivalent circuit that is illustrated in Figure 8c. The related values for $CH_3NH_3PbI_3/TiO_2$ and $NiO_x/CH_3NH_3PbI_3$ are reported in the second (d–f) and third (g–i) rows.

constant for light biasing voltage up to about 0.8 V and decreases rapidly for voltages more than this value. Therefore, we can attribute this voltage to the built-in potential at the $TiO_2/CH_3NH_3PbI_2$ interface that suppresses electron transfer from the mesoporous TiO_2 layer to the perovskite layer. The built-in potential for the 700 nm thick mesoporous TiO_2 layer in contact with $CH_3NH_3PbI_3$ is reported to be about 0.8 V in the literature, which is consistent with our results. The built-in potential at $NiO_x/CH_3NH_3PbI_2$ is a bit lower, but a rapid change of interfacial resistance is distinguishable between 0.65 and 0.8 V. $CH_3NH_3PbI_3$ was regarded as an intrinsic semiconductor in previous works,[60,67,68] so its density of charge carriers is highly influenced by its adjacent materials. PSCs were kept in open-circuit condition under different light intensities; therefore the DC current density is negligible. The materials are the same for three devices, so the built-in potentials are the same. The impedance at each point is a division of magnitude of small AC perturbation voltage (ΔV) and the measured current (ΔI). Formation of defects in the structure and interfaces result in decreasing ΔI and increasing the impedance.

As shown in Figure 10, the interfacial resistivities for perovskite/NiO_x and perovskite/TiO_2 in open-circuit voltages lower than the built-in potential are higher for 700 and 250 nm Al_2O_3 layers compared with the 450 nm Al_2O_3 layer. It seems that for large Al_2O_3 thickness, the number of surface defects is too large, while for small Al_2O_3 thickness, it may cause shunt paths. By increasing the light intensity, the resulting bias voltage overcomes the built-in potential that results in decreasing the barrier against transferring electrons from TiO_2 to $CH_3NH_3PbI_3$ and transferring holes from NiO_x to $CH_3NH_3PbI_3$. This would cause decreasing recombination resistance; therefore the meaning of interfacial resistance is different in this situation. Decreasing the carrier diffusion length due to the increasing recombination rate in higher carrier densities is also reported previously for single-crystal PSCs.[8] Time-resolved photoluminescence data (Figure 9) also show that PL lifetime for the perovskite inside a thick mesoporous Al_2O_3 layer is considerably shorter than that for perovskite/glass (52.5 ns versus 109.5 ns). This demonstrates that although Al_2O_3 is an insulator, it forms defects at the interface with the $CH_3NH_3PbI_3$ perovskite resulting in decreased lifetime and impedance at different parts of the PSC.

Figure 10 also indicates that the interfacial resistance remains constant in a wide V_{OC} range for the device made of the 450 nm Al_2O_3 layer, but those of 250 and 700 nm devices decrease continuously maybe due to the higher number of defects in these structures. We can interpret the measured time constant at voltages with lower values than V_{bi}–TiO_2 to the required time for charge transfer, but that of larger voltages to the lifetime. At lower voltages, open-circuit voltage is related to trapped electrons; therefore the lifetime is more related to higher voltages.[69] The related resistances for lower voltages can be a function of series resistance that is defined in Figure 8b, but those of higher voltages can be a function of shunt resistance defined in a DC model shown in Figure 8a.

It is indicated that high defect density is formed at the interface of the polycrystalline perovskite layer with its adjacent materials or at its surface. By increasing the thickness of the mesoporous spacer layer, the surface area increases significantly and results in increasing the number of defects. The higher charge transfer resistance in the case of PSCs with a thinner

DOI: 10.1021/acsami.7b02799
ACS Appl. Mater. Interfaces 2017, 9, 25204–25215

spacer layer (250 nm) may be attributed to undesired connections between the NiO_x/carbon layer and the TiO_2 layer, while the defects may increase in the case of PSCs with a thicker spacer layer (700 nm). The measured IPCE for these two cases are much smaller at the higher wavelengths due to the presence of these defects near the NiO_x layer (refer to Figures S3b and S7, SI). It is indicated that in a PSC with a single crystalline $CH_3NH_3PbI_3$ layer the absorbed wavelength range can be expanded up to 850 nm as a result of removing these defects.[8] Furthermore, an exciton absorption peak near 790 nm in the $CH_3NH_3PbI_3$ structure with large crystal sizes[8] was observed in the IPCE spectrum. This peak cannot be observed in our PSCs with the $CH_3NH_3PbI_3$ nanocrystals infiltrated in a mesoporous structure.

One of the most significant advantages of using a carbon mesoporous layer as the back electrode in the PSC structure is to protect the perovskite layer against humidity. In PSCs in which Ag is used instead of Au, fast degradation was observed and reported.[12,60,70] The AgI layer forms at the surface of Ag due to the reaction of Ag atoms with iodide ions diffused from $CH_3NH_3PbI_3$ or HI molecules produced by the following equation in the presence of water molecules:[65]

$$\begin{aligned} &H_2O + [(CH_3NH_3^+)PbI_3]_n \\ &\rightarrow [(CH_3NH_3^+)_{n-1}(CH_3NH_2)_nPbI_3][H_3O^+] \\ &\rightarrow HI + CH_3NH_2 + PbI_2 + H_2O + [(CH_3NH_3^+)PbI_3]_{n-1} \end{aligned} \quad (5)$$

Carbon is not degraded by iodide. Moreover, the thick layer of the carbon composite layer is filled by the perovskite layer. This 4−5 μm thick dense layer protects the main perovskite absorber layer against water molecules penetration. Our results show that the efficiency decreases from 11% to 9% after keeping the sample in humidity about 40% without any sealing for 3 months. Investigating the chemical stabilities in dark and light conditions are important issues that should be further studied.

4. CONCLUSION

NiO_x with valence band energy of about −5.4 to −5.6 eV and relatively good hole mobility is a good inorganic HTM for perovskite solar cells. A printable mesoporous $TiO_2/Al_2O_3/NiO_x$/carbon composite structure is a relatively low-cost, organic HTM-free and Au-free structure with greater enduring stability. Results indicated that depositing PbI_2 in 70 °C gives rise to holes formation in its structure that facilitate MAI penetration and $CH_3NH_3PbI_3$ formation. UV−O_3 treatment results in oxidizing Ni^{2+} to Ni^{3+} on the surface of mesoporous nickel oxide and enhances its semiconducting property that gives rise to a better charge extraction and an enhanced V_{oc} value. Electrochemical impedance spectral data show the lowest interfacial resistances at different interfaces for the PSCs with a 450 nm thick Al_2O_3 layer. In contrast, more defects inside the perovskite/Al_2O_3 composite layer may be produced for devices made of a thicker Al_2O_3 layer (700 nm), and more perovskite/Al_2O_3 interfacial defects may be produced for devices made of a thinner Al_2O_3 layer (200 nm); in either case lower *Voc* values were obtained. The lowest internal series resistance and higher shunt resistance were achieved for the device made of the Al_2O_3 layer with 450 nm thickness. The best device performance were obtained with the 450 nm device with PCE 12.12%, and the performance was retained above 80% for the devices stored in ambient air condition without encapsulation for more than 3 months.

■ ASSOCIATED CONTENT

Supporting Information

The Supporting Information is available free of charge on the ACS Publications website at DOI: 10.1021/acsami.7b02799.

SEM images of green and black nickel oxide layers and photovoltaic properties of devices that were made by them, effects of substrate and solution deposition temperature on photovoltaic properties of the cell and forward scans in comparison with backward scans, and result values for internal resistivities of the PSCs and also X-ray spectra (PDF)

■ AUTHOR INFORMATION

Corresponding Authors

*(F.B.) E-mail: behrouznejad@ncl.sharif.edu. Fax: +98-21-66022711. Tel.: +98-21-6616 4570.

*(E.W.-G.D.) E-mail: diau@mail.nctu.edu.tw. Fax: +886-3-5723764. Tel.: +886-3-5131524.

*(N.T.) E-mail: taghavinia@sharif.edu. Fax: +98-21-66022711. Tel.: +98-21-6616 4532.

ORCID

Eric W.-G. Diau: 0000-0001-6113-5679

Nima Taghavinia: 0000-0001-6815-2041

Notes

The authors declare no competing financial interest.

■ ACKNOWLEDGMENTS

This work was supported by Ministry of Science and Technology (MOST) of Taiwan (Grants MOST105-2119-M-009-011-MY3 and MOST 104-2119-M-009-001) and Sharif University of Technology. F.B. thanks National Chiao Tung University (Hsinchu, Taiwan) and Iranian Ministry of Science and Technology (Tehran, Iran) for support of her visit to NCTU. Financial and technical support by Sharif Solar Co. is also acknowledged.

■ ABBREVIATIONS

CPE, constant phase element
EDS, energy dispersion spectroscopy
EIS, electrochemical impedance spectra
HTM, hole-transporting materials
PSC, perovskite solar cell
XPS, X-ray photoelectron spectroscopy
XRD, X-ray diffraction

■ REFERENCES

(1) Stranks, S. D.; Snaith, H. J. Metal-Halide Perovskites for Photovoltaic and Light-Emitting Devices. *Nat. Nanotechnol.* **2015**, *10* (5), 391−402.

(2) Lin, Q.; Armin, A.; Chandra, R.; Nagiri, R.; Burn, P. L.; Meredith, P. Electro-optics of Perovskite Solar Cells. *Nat. Photonics* **2014**, *9* (2), 106−112.

(3) Nie, W.; Tsai, H.; Asadpour, R.; Blancon, J.-C.; Neukirch, A. J.; Gupta, G.; Crochet, J. J.; Chhowalla, M.; Tretiak, S.; Alam, M. A.; Wang, H.-L.; Mohite, A. D. High-Efficiency Solution-Processed Perovskite Solar Cells with Millimeter-Scale Grains. *Science* **2015**, *347* (6221), 522−525.

(4) Yuan, M.; Quan, L. N.; Comin, R.; Walters, G.; Sabatini, R.; Voznyy, O.; Hoogland, S.; Zhao, Y.; Beauregard, E. M.; Kanjanaboos,

DOI: 10.1021/acsami.7b02799
ACS Appl. Mater. Interfaces 2017, 9, 25204−25215

P.; Lu, Z.; Kim, D. H.; Sargent, E. H. Perovskite Energy Funnels for Efficient Light-Emitting Diodes. *Nat. Nanotechnol.* **2016**, *11* (10), 872−877.
(5) Li, G.; Rivarola, F. W. R.; Davis, N. J. L. K.; Bai, S.; Jellicoe, T. C.; de la Peña, F.; Hou, S.; Ducati, C.; Gao, F.; Friend, R. H.; Greenham, N. C.; Tan, Z.-K. Highly Efficient Perovskite Nanocrystal Light-Emitting Diodes Enabled by a Universal Crosslinking Method. *Adv. Mater.* **2016**, *28* (18), 3528−3534.
(6) Qin, P.; Paek, S.; Dar, M. I.; Pellet, N.; Ko, J.; Grätzel, M.; Nazeeruddin, M. K. Perovskite Solar Cells with 12.8% Efficiency by Using Conjugated Quinolizino Acridine Based Hole Transporting Material. *J. Am. Chem. Soc.* **2014**, *136* (24), 8516−8519.
(7) Jeon, N. J.; Noh, J. H.; Yang, W. S.; Kim, Y. C.; Ryu, S.; Seo, J.; Seok, S. Compositional Engineering of Perovskite Materials for High-Performance Solar Cells. *Nature* **2015**, *517*, 476−480.
(8) Dong, Q.; Fang, Y.; Shao, Y.; Mulligan, P.; Qiu, J.; Cao, L.; Huang, J. Electron-Hole Diffusion Lengths > 175 μm in Solution-Grown $CH_3NH_3PbI_3$ Single Crystals. *Science* **2015**, *347* (6225), 967−970.
(9) Stranks, S. D.; Eperon, G. E.; Grancini, G.; Menelaou, C.; Alcocer, M. J. P.; Leijtens, T.; Herz, L. M.; Petrozza, A.; Snaith, H. J. Electron-Hole Diffusion Lengths Exceeding 1 Micrometer in an Organometal Trihalide Perovskite Absorber. *Science* **2013**, *342* (6156), 341−344.
(10) Leijtens, T.; Stranks, S. D.; Eperon, G. E.; Lindblad, R.; Johansson, E. M. J.; McPherson, I. J.; Rensmo, H.; Ball, J. M.; Lee, M. M.; Snaith, H. J. Electronic Properties of Meso-Superstructured and Planar Organometal Halide Perovskite Films: Charge Trapping, Photodoping, and Carrier Mobility. *ACS Nano* **2014**, *8* (7), 7147−7155.
(11) Noh, J. H.; Im, S. H.; Heo, J. H.; Mandal, T. N.; Seok, S. Il. Chemical Management for Colorful, Efficient, and Stable Inorganic-Organic Hybrid Nanostructured Solar Cells. *Nano Lett.* **2013**, *13* (4), 1764−1769.
(12) Kato, Y.; Ono, L. K.; Lee, M. V.; Wang, S.; Raga, S. R.; Qi, Y. Silver Iodide Formation in Methyl Ammonium Lead Iodide Perovskite Solar Cells with Silver Top Electrodes. *Adv. Mater. Interfaces* **2015**, *2* (13), 1500195.
(13) Xiao, Z.; Yuan, Y.; Shao, Y.; Wang, Q.; Dong, Q.; Bi, C.; Sharma, P.; Gruverman, A.; Huang, J. Giant Switchable Photovoltaic Effect in Organometal Trihalide Perovskite Devices. *Nat. Mater.* **2014**, *14* (2), 193−198.
(14) Chen, H.; Wei, Z.; He, H.; Zheng, X.; Wong, K. S.; Yang, S. Solvent Engineering Boosts the Efficiency of Paintable Carbon-Based Perovskite Solar Cells to Beyond 14%. *Adv. Energy Mater.* **2016**, *6* (8), 1502087.
(15) Laban, W. A.; Etgar, L. Depleted Hole Conductor-Free Lead Halide Iodide Heterojunction Solar Cells. *Energy Environ. Sci.* **2013**, *6* (11), 3249−3253.
(16) Zhou, X.; Bao, C.; Li, F.; Gao, H.; Yu, T.; Yang, J.; Zhu, W.; Zou, Z. Hole-Transport-Material-Free Perovskite Solar Cells Based on Nanoporous Gold Back Electrode. *RSC Adv.* **2015**, *5* (72), 58543−58548.
(17) Liu, Y.; Ji, S.; Li, S.; He, W.; Wang, K.; Hu, H.; Ye, C. Study on Hole-Transport-Material-Free Planar $TiO_2/CH_3NH_3PbI_3$ Heterojunction Solar Cells: The Simplest Configuration of a Working Perovskite Solar Cell. *J. Mater. Chem. A* **2015**, *3* (28), 14902−14909.
(18) Shi, J.; Luo, Y.; Wei, H.; Luo, J.; Dong, J.; Lv, S.; Xiao, J.; Xu, Y.; Zhu, L.; Xu, X.; Wu, H.; Li, D.; Meng, Q. Modified Two-Step Deposition Method for High-Efficiency TiO $_2$ /CH $_3$ NH $_3$ PbI $_3$ Heterojunction Solar Cells. *ACS Appl. Mater. Interfaces* **2014**, *6* (12), 9711−9718.
(19) Kay, A.; Grätzel, M. Low Cost Photovoltaic Modules Based on Dye Sensitized Nanocrystalline Titanium Dioxide and Carbon Powder. *Sol. Energy Mater. Sol. Cells* **1996**, *44* (1), 99−117.
(20) Ku, Z.; Rong, Y.; Xu, M.; Liu, T.; Han, H. Full Printable Processed Mesoscopic $CH_3NH_3PbI_3/TiO_2$ Heterojunction Solar Cells with Carbon Counter Electrode. *Sci. Rep.* **2013**, *3*, 3132.
(21) Chan, C.-Y.; Wang, Y.; Wu, G.-W.; Diau, E. W.-G. Solvent-Extraction Crystal Growth for Highly Efficient Carbon-Based Mesoscopic Perovskite Solar Cells Free of Hole Conductors. *J. Mater. Chem. A* **2016**, *4* (10), 3872−3878.
(22) Chen, J.; Rong, Y.; Mei, A.; Xiong, Y.; Liu, T.; Sheng, Y.; Jiang, P.; Hong, L.; Guan, Y.; Zhu, X.; Hou, X.; Duan, M.; Zhao, J.; Li, X.; Han, H. Hole-Conductor-Free Fully Printable Mesoscopic Solar Cell with Mixed-Anion Perovskite $CH_3NH_3PbI_{(3-x)}(BF_4)_x$. *Adv. Energy Mater.* **2016**, *6* (5), 1502009.
(23) Li, H.; Cao, K.; Cui, J.; Liu, S.; Qiao, X.; Shen, Y.; Wang, M. 14.7% Efficient Mesoscopic Perovskite Solar Cells Using Single Walled Carbon Nanotubes/Carbon Composite Counter Electrodes. *Nanoscale* **2016**, *8* (12), 6379−6385.
(24) Liu, Z.; Zhang, M.; Xu, X.; Cai, F.; Yuan, H.; Bu, L.; Li, W.; Zhu, A.; Zhao, Z.; Wang, M.; Cheng, Y.-B.; He, H. NiO Nanosheets as Efficient Top Hole Transporters for Carbon Counter Electrode Based Perovskite Solar Cells. *J. Mater. Chem. A* **2015**, *3* (47), 24121−24127.
(25) Xu, M.; Rong, Y.; Ku, Z.; Mei, A.; Liu, T.; Zhang, L.; Li, X.; Han, H. Highly Ordered Mesoporous Carbon for Mesoscopic $CH_3NH_3PbI_3/TiO_2$ Heterojunction Solar Cell. *J. Mater. Chem. A* **2014**, *2* (23), 8607−8611.
(26) Tsai, C.-M.; Wu, G.-W.; Narra, S.; Chang, H.-M.; Mohanta, N.; Wu, H.-P.; Wang, C.-L.; Diau, E. W.-G. Control of Preferred Orientation with Slow Crystallization for Carbon-Based Mesoscopic Perovskite Solar Cells Attaining Efficiency 15%. *J. Mater. Chem. A* **2017**, *5* (2), 739−747.
(27) Zhou, H.; Shi, Y.; Wang, K.; Dong, Q.; Bai, X.; Xing, Y.; Du, Y.; Ma, T. Low-Temperature Processed and Carbon-Based ZnO/$CH_3NH_3PbI_3$/C Planar Heterojunction Perovskite Solar Cells. *J. Phys. Chem. C* **2015**, *119* (9), 4600−4605.
(28) Wei, Z.; Chen, H.; Yan, K.; Yang, S. Inkjet Printing and Instant Chemical Transformation of a $CH_3NH_3PbI_3$/Nanocarbon Electrode and Interface for Planar Perovskite Solar Cells. *Angew. Chem., Int. Ed.* **2014**, *53* (48), 13239−13243.
(29) Wei, Z.; Yan, K.; Chen, H.; Yi, Y.; Zhang, T.; Long, X.; Li, J.; Zhang, L.; Wang, J.; Yang, S. Cost-Efficient Clamping Solar Cells Using Candle Soot for Hole Extraction from Ambipolar Perovskites. *Energy Environ. Sci.* **2014**, *7* (10), 3326−3333.
(30) Li, Z.; Kulkarni, S. a; Boix, P. P.; Shi, E.; Cao, A.; Fu, K.; Batabyal, S. K.; Zhang, J.; Xiong, Q.; Wong, L. H.; Mathews, N.; Mhaisalkar, S. G. Laminated Carbon Nanotube Networks for Metal Electrode-Free Efficient Perovskite Solar Cells. *ACS Nano* **2014**, *8* (7), 6797−6804.
(31) Habisreutinger, S. N.; Leijtens, T.; Eperon, G. E.; Stranks, S. D.; Nicholas, R. J.; Snaith, H. J. Carbon Nanotube/Polymer Composites as a Highly Stable Hole Collection Layer in Perovskite Solar Cells. *Nano Lett.* **2014**, *14* (10), 5561−5568.
(32) Habisreutinger, S. N.; Leijtens, T.; Eperon, G. E.; Stranks, S. D.; Nicholas, R. J.; Snaith, H. J. Enhanced Hole Extraction in Perovskite Solar Cells through Carbon Nanotubes. *J. Phys. Chem. Lett.* **2014**, *5* (23), 4207−4212.
(33) Cao, J.; Liu, Y.-M.; Jing, X.; Yin, J.; Li, J.; Xu, B.; Tan, Y.-Z.; Zheng, N. Well-Defined Thiolated Nanographene as Hole-Transporting Material for Efficient and Stable Perovskite Solar Cells. *J. Am. Chem. Soc.* **2015**, *137* (34), 10914−10917.
(34) You, J.; Meng, L.; Song, T.-B.; Guo, T.-F.; Yang, Y. M.; Chang, W.-H.; Hong, Z.; Chen, H.; Zhou, H.; Chen, Q.; Liu, Y.; De Marco, N.; Yang, Y. (Michael). Improved Air Stability of Perovskite Solar Cells via Solution-Processed Metal Oxide Transport Layers. *Nat. Nanotechnol.* **2015**, *11*, 75−81.
(35) Jeng, J.; Chen, K.; Chiang, T.; Lin, P.; Tsai, T.; Chang, Y.; Guo, T.; Chen, P.; Wen, T.; Hsu, Y. Nickel Oxide Electrode Interlayer in CH 3 NH 3 PbI 3 Perovskite/PCBM Planar-Heterojunction Hybrid Solar Cells. *Adv. Mater.* **2014**, *26*, 4107−4113.
(36) Xu, X.; Liu, Z.; Zuo, Z.; Zhang, M.; Zhao, Z.; Shen, Y.; Zhou, H.; Chen, Q.; Yang, Y.; Wang, M. Hole Selective NiO Contact for Efficient Perovskite Solar Cells with Carbon Electrode. *Nano Lett.* **2015**, *15* (4), 2402−2408.

DOI: 10.1021/acsami.7b02799
ACS Appl. Mater. Interfaces 2017, 9, 25204−25215

(37) Zhu, S.; Shan, L.; Tian, X.; Zheng, X.; Sun, D.; Liu, X.; Wang, L.; Zhou, Z. Hydrothermal Synthesis of Oriented ZnO Nanorod-Nanosheets Hierarchical Architecture on Zinc Foil as Flexible Photoanodes for Dye-Sensitized Solar Cells. *Ceram. Int.* **2014**, *40*, 11663−11670.
(38) Cao, K.; Zuo, Z.; Cui, J.; Shen, Y.; Moehl, T.; Zakeeruddin, S. M.; Grätzel, M.; Wang, M. Efficient Screen Printed Perovskite Solar Cells Based on Mesoscopic TiO_2/Al_2O_3/NiO/carbon Architecture. *Nano Energy* **2015**, *17*, 171−179.
(39) Kwon, U.; Kim, B.-G.; Nguyen, D. C.; Park, J.-H.; Ha, N. Y.; Kim, S.-J.; Ko, S. H.; Lee, S.; Lee, D.; Park, H. J. Solution-Processible Crystalline NiO Nanoparticles for High-Performance Planar Perovskite Photovoltaic Cells. *Sci. Rep.* **2016**, *6*, 30759.
(40) Sepalage, G. a.; Meyer, S.; Pascoe, A.; Scully, A. D.; Huang, F.; Bach, U.; Cheng, Y.-B.; Spiccia, L. Copper(I) Iodide as Hole-Conductor in Planar Perovskite Solar Cells: Probing the Origin of J - V Hysteresis. *Adv. Funct. Mater.* **2015**, *25* (35), 5650−5661.
(41) Qin, P.; Tanaka, S.; Ito, S.; Tetreault, N.; Manabe, K.; Nishino, H.; Nazeeruddin, M. K.; Grätzel, M. Inorganic Hole Conductor-Based Lead Halide Perovskite Solar Cells with 12.4% Conversion Efficiency. *Nat. Commun.* **2014**, *5*, 3834.
(42) Ye, S.; Sun, W.; Li, Y.; Yan, W.; Peng, H.; Bian, Z.; Liu, Z.; Huang, C. CuSCN-Based Inverted Planar Perovskite Solar Cell with an Average PCE of 15.6%. *Nano Lett.* **2015**, *15* (6), 3723−3728.
(43) Yan, W.; Ye, S.; Li, Y.; Sun, W.; Rao, H.; Liu, Z.; Bian, Z.; Huang, C. Hole-Transporting Materials in Inverted Planar Perovskite Solar Cells. *Adv. Energy Mater.* **2016**, *6* (17), 1600474.
(44) Liu, Z.; Zhang, fM.; Xu, X.; Cai, F.; Yuan, H.; Bu, L.; Li, W.; Zhu, A.; Zhao, Z.; Wang, M.; Cheng, Y.-B.; He, H. NiO Nanosheets as Efficient Top Hole Transporters for Carbon Counter Electrode Based Perovskite Solar Cells. *J. Mater. Chem. A* **2015**, *3*, 24121−24127.
(45) Nakae, N.; Ishisada, J.; Shirai, K.; Yanase, A. Fermi Surface and Metallic Properties of Graphite at High Pressures. *J. Phys. Chem. Solids* **2010**, *71* (4), 418−422.
(46) Marulanda, J. M.; Srivastava, A. Carrier Density and Effective Mass Calculations in Carbon Nanotubes. *Phys. Status Solidi B* **2008**, *245* (11), 2558−2562.
(47) Shiraishi, M.; Ata, M. Work Function of Carbon Nanotubes. *Carbon* **2001**, *39*, 1913−1917.
(48) Chan, L. H.; Hong, K. H.; Xiao, D. Q.; Hsieh, W. J.; Lai, S. H.; Shih, H. C.; Lin, T. C.; Shieu, F. S.; Chen, K. J.; Cheng, H. C. Role of Extrinsic Atoms on the Morphology and Field Emission Properties of Carbon Nanotubes. *Appl. Phys. Lett.* **2003**, *82* (24), 4334−4336.
(49) Palanna, O. G. *Engineering Chemistry*; Tata McGraw-Hill Education: New Delhi, 2009; Chapter 11, pp 408−409.
(50) Dueñas, S.; Castán, H.; García, H.; Andrés, E. S.; Toledano-Luque, M.; Mártil, I.; González-Díaz, G.; Kukli, K.; Uustare, T.; Aarik, J. A Comparative Study of the Electrical Properties of TiO 2 Films Grown by High-Pressure Reactive Sputtering and Atomic Layer Deposition. *Semicond. Sci. Technol.* **2005**, *20* (10), 1044−1051.
(51) Quarti, C.; Mosconi, E.; De Angelis, F. Interplay of Orientational Order and Electronic Structure in Methylammonium Lead Iodide: Implications for Solar Cell Operation. *Chem. Mater.* **2014**, *26* (22), 6557−6569.
(52) Choi, S. C.; Koumoto, K.; Yanagida, H. Electrical Conduction and Effective Mass of a Hole in Single-Crystal NiO. *J. Mater. Sci.* **1986**, *21* (6), 1947−1950.
(53) Lee, H. K.; Kim, J.-K.; Park, O. O. Effects of UV Light-Irradiated Buffer Layer on the Performance of Polymer Solar Cells. *Org. Electron.* **2009**, *10* (8), 1641−1644.
(54) Kim, J.; Lee, H. R.; Kim, H. P.; Lin, T.; Kanwat, A.; Mohd Yusoff, A. R.; Jang, J. Effects of UV-Ozone Irradiation on Copper Doped Nickel Acetate and Its Applicability to Perovskite Solar Cells. *Nanoscale* **2016**, *8* (17), 9284−9292.
(55) Liu, S.; Liu, R.; Chen, Y.; Ho, S.; Kim, J. H.; So, F. Nickel Oxide Hole Injection/transport Layers for Efficient Solution-Processed Organic Light-Emitting Diodes. *Chem. Mater.* **2014**, *26* (15), 4528−4534.
(56) Noonuruk, R.; Wongpisutpaisan, N.; Mukdacharoenchai, P.; Techitdheera, W.; Pecharapa, W. Ozone-Induced Optical Density Change of NiO Thin Films and Their Applicability as Neutral Optical Density Filter. *Procedia Eng.* **2011**, *8*, 212−216.
(57) Zaky, A. M.; Assaf, F. H.; Ali, F. E. Z. A. H. Electrochemical Behavior of Zn-Ni Alloys in Borate Buffer Solutions. *ISRN Mater. Sci.* **2011**, *2011*, 356863.
(58) Reddy, Y. A. K. Influence of Growth Temperature on the Properties of DC Reactive Magnetron Sputtered NiO Thin Films. *Int. J. Curr. Eng. Technol.* **2013**, *2* (2), 351−357.
(59) Liu, Z.; Helander, M. G.; Wang, Z.; Lu, Z. Band Alignment at Anode/Organic Interfaces for Highly Efficient Simplified Blue-Emitting Organic Light-Emitting Diodes. *J. Phys. Chem. C* **2010**, *114* (39), 16746−16749.
(60) Behrouznejad, F.; Shahbazi, S.; Taghavinia, N.; Wu, H.-P.; Diau, E. W.-G. A Study on Utilizing Different Metals as the Back Contact of $CH_3NH_3PbI_3$ Perovskite Solar Cells. *J. Mater. Chem. A* **2016**, *4* (35), 13488−13498.
(61) Behrouznejad, F.; Taghavinia, N. Utilizing Chromium as the Photoanode Substrate in Dye-Sensitized Solar Cells. *ChemElectroChem* **2014**, *1* (5), 944−950.
(62) Behrouznejad, F.; Taghavinia, N. High-Performance/low-Temperature-Processed Dye Solar Cell Counter Electrodes Based on Chromium Substrates with Cube-like Morphology. *J. Power Sources* **2014**, *260*, 299−306.
(63) Behrouznejad, F.; Taghavinia, N.; Pazoki, M.; Tajabadi, F. Metal-Based Bracken-like Single-Sided Dye- Sensitized Solar Cells with Horizontal Separation. *Phys. Chem. Chem. Phys.* **2016**, *18*, 5244−5252.
(64) Shi, D.; Qin, X.; Li, Y.; He, Y.; Zhong, C.; Pan, J.; Dong, H.; Xu, W.; Li, T.; Hu, W.; Bredas, J.-L.; Bakr, O. M. Spiro-OMeTAD Single Crystals: Remarkably Enhanced Charge-Carrier Transport via Mesoscale Ordering. *Sci. Adv.* **2016**, *2* (4), e1501491−e1501491.
(65) Frost, J. M.; Butler, K. T.; Brivio, F.; Hendon, C. H.; van Schilfgaarde, M.; Walsh, A. Atomistic Origins of High-Performance in Hybrid Halid Perovskite Solar Cells. Nano Lett. 14, 2584−90 (2014).e in Hybrid Halide Perovskite Solar Cells. *Nano Lett.* **2014**, *14* (5), 2584−2590.
(66) Yang, Y.; Xiao, J.; Wei, H.; Zhu, L.; Li, D.; Luo, Y.; Wu, H.; Meng, Q. An All-Carbon Counter Electrode for Highly Efficient Hole-Conductor-Free Organo-Metal Perovskite Solar Cells. *RSC Adv.* **2014**, *4* (95), 52825−52830.
(67) Miyano, K.; Tripathi, N.; Yanagida, M.; Shirai, Y. Lead Halide Perovskite Photovoltaic as a Model P − I − N Diode. *Acc. Chem. Res.* **2016**, *49* (2), 303−310.
(68) Walsh, A.; Scanlon, D. O.; Chen, S.; Gong, X. G.; Wei, S. Self-Regulation Mechanism for Charged Point Defects in Hybrid Halide Perovskites. *Angew. Chem., Int. Ed.* **2015**, *54* (6), 1791−1794.
(69) Sanchez, R. S.; Gonzalez-Pedro, V.; Lee, J. W.; Park, N. G.; Kang, Y. S.; Mora-sero, I.; Bisquert, J. Slow Dynamic Processes in Lead Halide Perovskite Solar Cells. Characteristic Times and Hysteresis. *J. Phys. Chem. Lett.* **2014**, *5* (13), 2357−2363.
(70) Leijtens, T.; Eperon, G. E.; Pathak, S.; Abate, A.; Lee, M. M.; Snaith, H. J. Overcoming Ultraviolet Light Instability of Sensitized TiO2 with Meso-Superstructured Organometal Tri-Halide Perovskite Solar Cells. *Nat. Commun.* **2013**, *4*, 2885.

DOI: 10.1021/acsami.7b02799
ACS Appl. Mater. Interfaces 2017, 9, 25204−25215